

Radial gradients in PET monofilaments: A Raman mapping and SAXS tomography study

E. Perret^{a,b,*}, K. Chen^{a,c}, O. Braun^{d,e}, R. Muff^d, R. Hufenus^a

^a Laboratory for Advanced Fibers, Empa, Swiss Federal Laboratories for Materials Science and Technology, Lerchenfeldstrasse 5, 9014, St. Gallen, Switzerland

^b Center for X-ray Analytics, Empa, Swiss Federal Laboratories for Materials Science and Technology, Überlandstrasse 129, 8600, Dübendorf, Switzerland

^c State Key Laboratory for Modification of Chemical Fibers and Polymer Materials, College of Materials Science and Engineering, Donghua University, Shanghai, 201620, China

^d Transport at Nanoscale Interfaces Laboratory, Empa, Swiss Federal Laboratories for Materials Science and Technology, Überlandstrasse 129, 8600, Dübendorf, Switzerland

^e Department of Physics, University of Basel, Klingelbergstrasse 82, 4056, Basel, Switzerland

ARTICLE INFO

Keywords:

Raman mapping
PET
Radial gradients
SAXS
Tomography

ABSTRACT

Surface properties of monofilaments can be tailored with radial structural gradients, which is of specific interest for technical textile applications. Radial gradients in fine ($\leq 40 \mu\text{m}$ thick) poly(ethylene terephthalate) monofilaments have been studied with high-resolution Raman mapping and one-dimensional microbeam small-angle x-ray scattering tomography. Filaments have been melt-spun by using online and offline drawing techniques. Radial structural gradients are strongly affected by the drawing method. Raman mapping revealed that offline drawn filaments have a higher crystallinity in the core than in the surface region, whereas the opposite is the case for online drawn filaments. The molecular alignment was the highest in the core for all filaments. Microbeam SAXS tomography revealed that the long-spacing between crystals, in the direction of the fiber axis, increases towards the fiber surface. Fibers that have been drawn to a larger extent, resulting in improved tensile strength, have been found to have a larger long-spacing.

1. Introduction

Poly(ethylene terephthalate) is the most used polymer for melt-spun fibers in the textile industry due to its excellent physical properties and low price. Thus, the global demand for PET fibers is still rising every year. PET fibers are used in sectors like home furnishing, filtration, automotive or technical textiles [1]. For technical textiles, the radial structure is of particular interest, since it affects tensile properties and surface characteristics like abrasion resistance of the fiber. However, it is very challenging to extract radial structural gradients in fine (26–40 μm thick) polymer fibers. One dimensional gradients can be detected by e.g. 1D small-angle x-ray scattering (SAXS) tomography or wide-angle x-ray diffraction tomography [2–6]. The major disadvantages of 1D tomography methods are (a) that they rely on the assumption that the fibers are radially symmetric and (b) that the signal-to-noise ratio is often very low in reconstructed tomography images due to the fineness of the fibers. Other methods to obtain one-dimensional gradients are for

example polarized light microscopy [7] and conventional Raman spectroscopy [8]. The disadvantage of the latter techniques is that the signal is averaged over the depth of the measured filament region, resulting in a smeared 1D profile. Two-dimensional information about fiber cross-sections, on the other hand, is challenging to obtain. A possible technique is e.g. 2D SAXS tomography, where the sample is rotated while taking images. Here, the major disadvantages are (a) the complexity of the measurements, (b) the amount of data obtained for analysis and (c) that the measurement has to be performed at a synchrotron. In contrast, the confocal 2D Raman mapping has been shown to be an ideal laboratory tool to study the radial structure (crystallinity, molecular alignment) in PET fiber cross-sections [9]. With already developed Python codes in place, the analysis of Raman data becomes rather rapid and feasible.

In this article, we have investigated the effect of the drawing method on the radial structural gradient of fine PET filament cross-sections with 2D Raman mapping and 1D SAXS tomography. A detailed 2D Raman

* Corresponding author. Laboratory for Advanced Fibers, Empa, Swiss Federal Laboratories for Materials Science and Technology, Lerchenfeldstrasse 5, 9014, St. Gallen, Switzerland.

E-mail address: edith.perret@empa.ch (E. Perret).

<https://doi.org/10.1016/j.polymer.2021.124422>

Received 27 September 2021; Received in revised form 18 November 2021; Accepted 29 November 2021

Available online 1 December 2021

0032-3861/© 2021 The Authors. Published by Elsevier Ltd. This is an open access article under the CC BY license (<http://creativecommons.org/licenses/by/4.0/>).

Table 1

Fiber labels, article numbers (Monosuisse AG), drawing method, material, fiber fineness (tex = mg/m), diameters and draw ratios.

Fiber labels	Article numbers	Drawing	Material	Fineness (dtex)	Diameter (μm)	DR
2s-26	11ZS0262026001	2-step	Grisuten	7	26	4.6
2s-35	11ZS0180026001	2-step	Grisuten	14	35	4.6
2s-40	11ZS0262035001	2-step	Grisuten	17	40	4.6
1s-26	11U31810035001	1-step	RT20	7	26	5.1
1s-35	11ZS0262040001	1-step	RT20	14	35	5.2
1s-40	11U31810040001	1-step	RT20	17	40	5.2

mapping analysis of the crystallinity and molecular alignment in fine ($\leq 40 \mu\text{m}$) PET filament cross-sections is presented. 1D SAXS tomography was used to extract complementary information about e.g. long-spacings between crystals and crystal tilts.

2. Experimental

2.1. Materials

PET monofilaments were provided by Monosuisse AG (Emmenbrücke, Switzerland). Drawn monofilaments have been achieved by a 2-step drawing technique, where an as-spun monofilament was drawn offline over a heating plate. Also, a 1-step drawing technique was applied, where monofilaments were drawn online during the melt-spinning procedure. Two different types of PET pellets have been used, Grisuten (Märkische Faser GmbH, Premnitz, Germany) and RT20 (Invista, Wichita, Kansas, United States). Pellets have been post-condensated (heated under vacuum) to achieve an intrinsic viscosity of about 0.99 dl/g for Grisuten and 0.95 dl/g for RT20. The spin pack had a temperature of 312 °C and consisted of a spinneret which had 8 capillaries for the 2-step drawn fibers and 16 capillaries for the 1-step drawn fibers. Each capillary die had a diameter of 0.45 mm and a length of 1.35 mm (for $\phi = 35 \mu\text{m}$, 40 μm fibers), or a diameter of 0.25 mm and a length of 0.75 mm (for $\phi = 26 \mu\text{m}$ fibers), respectively. The drawing technique, raw materials, fineness, diameters and draw ratios are summarized in Table 1. The draw ratio (DR) is the ratio between the winder speed and the take-up godet speed.

2.2. Characterization

2.2.1. High-resolution Raman mapping

PET fibers have been embedded in a resin hardener (Epoxy cure 2, Buehler, USA) following the procedure described elsewhere [10]. High-resolution (spatial resolution $<1 \mu\text{m}$) Raman maps have been

measured with a WITec Alpha 300 R confocal Raman microscope (WITec GmbH, Ulm, Germany) in backscattering geometry at Empa (Dübendorf, Switzerland). A blue laser with a 488 nm wavelength was, after passing a lambda-halfplate for linear polarization, focused onto the embedded sample using a 100 \times objective with a numerical aperture of 0.9. The diffraction-limited in-plane laser spot size is below 1 μm and the confocality of the Raman microscope limits the focal depth to approximately $<1 \mu\text{m}$. The laser power was set to 5 mW and the integration time for each spectrum was 0.4 s for all filaments. These settings ensured that no heating damage occurred in the samples due to the laser. A 300 mm lens-based spectrometer with a grating of 1800 g/mm and a thermoelectrically cooled CCD was used to analyze the backscattered light. Note that in the backscattered light no polarization selection was performed and that the Rayleigh scattered light was blocked by a notch filter.

The embedded samples were mounted onto a piezo stage and were scanned through the laser. Typically, an area of 40 \times 40 μm was mapped with 80 \times 80 lines, and for thicker samples an area of 45 \times 45 μm was mapped with 90 \times 90 lines. The measured spectra have been treated with a cosmic ray removal procedure and background was subtracted using the WITec Project Five (version 5.1, WITec GmbH, Ulm, Germany) software. All cosmic ray and background corrected Raman spectra were subsequently binned by averaging over 4 spectra (2×2), spanning an area of 1 μm^2 . The binned spectra were then normalized by the intensities of the 1291 cm^{-1} Raman band. The same data treatment has already successfully been applied to other PET fibers in the past [9].

Python codes have specifically been developed to fit Raman bands. Best fits have been achieved by fitting the bands to split-Pearson VII functions and a linear background. The split-Pearson VII sums up two Pearson VII functions. The intensity curve is split into two parts, one on the left side and one on the right side of the peak's maximum. Each side is fitted with a Pearson VII function, which is a Lorentzian function raised to the power m (shape factor) and is given by the following equation.

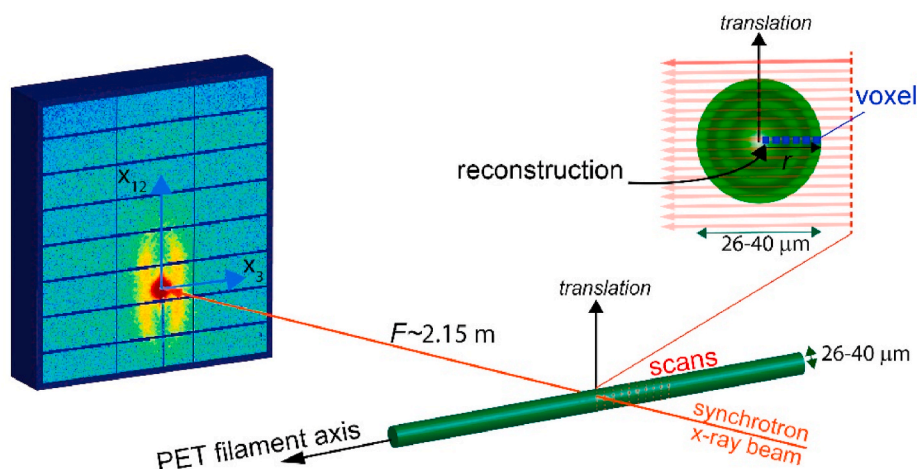


Fig. 1. Microbeam SAXS tomography setup. Inset: View of face of the fiber. Translation of the fiber through x-ray beam (red arrows). Through reconstruction, one obtains the structural information in the voxels (blue) at a distance r from the center. (For interpretation of the references to colour in this figure legend, the reader is referred to the Web version of this article.)

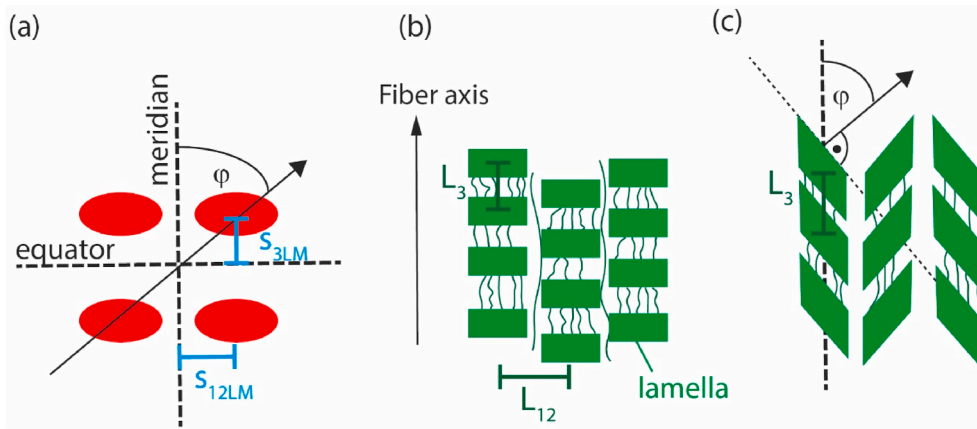


Fig. 2. (a) Four-point SAXS pattern and corresponding structural models: (b) checkerboard model (c) tilted lamellae.

$$I_{sim}^{Raman} = I \frac{FWHM^{2m}}{[FWHM^2 + (2^{1/m} - 1)(x - x_0)^2]^m} \quad (\text{Eq. 1})$$

The crystallinity χ^{Raman} of the PET fiber cross-sections determined with Raman spectroscopy was calculated using the following equation [9]:

$$\chi^{Raman} (\%) = \frac{I_{1097} - I_{1097a}}{I_{1120} + I_{1097}} \times 100 \quad (\text{Eq. 2})$$

where I_{1097} and I_{1120} are the measured intensities (peak heights) of the 1097 cm^{-1} and 1120 cm^{-1} peaks of the sample of interest. I_{1097a} is the intensity of the 1097 cm^{-1} vibration band of a 100% amorphous sample. In PET, the *trans* ethylene glycol conformation and thus the I_{1097} peak is also present in a 100% amorphous sample, and therefore its intensity contribution, I_{1097a} , has to be subtracted from the intensity contribution of the semi-crystalline sample, I_{1097} . The I_{1097a} was estimated to be about 0.17 by comparing the calculated crystallinities with values obtained from differential scanning calorimetry.

2.2.2. Microbeam SAXS tomography

One-dimensional microbeam SAXS tomography measurements have been performed at the cSAXS beamline at the Swiss Light Source synchrotron of the Paul Scherrer Institute in Switzerland. All monofilaments have been mounted horizontally onto a support, which has been attached to a piezo stage. An evacuated, 2.1 m long flight tube was positioned in-between the sample mount and the Pilatus 2 M detector [11] in order to reduce air-scattering. The monofilaments were translated step-wise ($1.25 \mu\text{m}$ steps) through a micrometer-sized (horizontal: $30 \mu\text{m}$, vertical: $5 \mu\text{m}$) x-ray beam. A Fresnel zone-plate was used to achieve such a small beam size and a monochromator was used to tune the energy of the x-ray beam to 11.2 keV . One scan of a monofilament through the x-ray beam resulted in 100 SAXS images with 1s exposures. For each filament, the scans have been repeated 10 times, except for fiber 1s-35, where the scans have been repeated 20 times. The monofilaments have been displaced side-wise by $40 \mu\text{m}$ in-between each scan (Fig. 1). A transmission diode, which was mounted in the beamstop, allowed to reliably find the center of the fiber for each scan.

SAXS patterns have been assigned to distinct volumes (voxels) within the fiber cross-section by applying a one-dimensional tomographic reconstruction by means of the inverse Abel transformation [12] (inset Fig. 1). The reconstruction algorithm is based on the assumption that the filaments have radial symmetry and can be accomplished by a matrix-vector multiplication with either the two-point Abel deconvolution or the Basex Abel transform method [5,6]. We have used the same Matlab codes that have already been successfully applied for the one-dimensional tomographic reconstruction of polyamide 6 monofilaments [2]. All images shown in the result section have been centered

and cropped to a square around the direct beam position ($|s_{12}, s_3| < 0.3 \text{ nm}^{-1}$), followed by transposing the images so that the meridian (s_3 , parallel to fiber axis) is vertical (unlike the image shown in Fig. 1). Additional data treatment had to be done before applying the reconstruction algorithms to the images. These details are given in the supporting information (SI section 3.1).

The momentum transfers, s_{12} and s_3 , are calculated using the following equations, where x_{12} denotes the horizontal distance of the pixel centers to the direct beam position, x_3 denotes the vertical distance (parallel to fiber axis) of the pixel centers to the direct beam position, $\lambda = 1.1 \text{ \AA}$ is the wavelength of the x-rays, and $F = 2.152 \text{ m}$ is the sample to detector distance.

$$s_{12} = \frac{x_{12}}{\lambda F}, \quad (\text{Eq. 3})$$

$$s_3 = \frac{x_3}{\lambda F} \quad (\text{Eq. 4})$$

In order to improve the signal-to-noise ratio, radially neighbouring four-point reconstructed and symmetrized (around the equator) SAXS patterns have been averaged. These binned images have then been projected onto the longitudinal s_3 axis (along the fiber axis, meridian), and onto the transversal s_{12} axis (perpendicular to fiber axis), respectively [3]. The corresponding equations for the projections are given below.

$$I(s_3) = 2\pi \int_0^\infty s_{12} I(s_{12}, s_3) ds_{12} \quad (\text{Eq. 5})$$

$$I(s_{12}) = 2 \int_0^\infty I(s_{12}, s_3) ds_3 \quad (\text{Eq. 6})$$

In case of the transversal projection, only the data in a horizontal slab around the upper two reflections was projected onto s_{12} , to avoid the high intensity of the direct beam. Fitting examples are shown in the supporting information (SI Figs. 4 and 5).

Structural information is extracted from the projections as follows. Two models can explain the observed four-point SAXS pattern (Fig. 2a) of PET filaments. The first model (checkerboard model) consists of a macro-lattice, where lamellae (crystals) are stacked along the fiber axis, having a longspacing of L_3 [13,14]. These stacks of lamellae form microfibrils, which have a transverse distance of L_{12} (Fig. 2b). The second model (tilted lamellae model) consists of a macro-lattice with lamellae that are tilted away from the filament axis by an angle, ϕ (Fig. 2c) [15, 16].

The average long-spacing, $L_3 = |1/s_{3LM}|$, between lamellae along the fiber axis was determined by fitting the symmetrized longitudinal

Table 2

Assignments of Raman bands to vibrations in PET [17–20].

Peak position	Assignment
1097 cm ⁻¹	Ring C–C, ester C(O)–O, ethylene glycol C–C stretching (<i>trans</i>)
1120 cm ⁻¹	Ring C–H in-plane bending, ester C(O)–O and ethylene glycol C–C stretching (<i>gauche</i>)
1291 cm ⁻¹	Ring and O–C stretching (used for normalization)
1616 cm ⁻¹	C–C/C=C benzene ring mode 8a (Wilson notation [21])
1729 cm ⁻¹	C=O stretching

projections to Pearson VII functions, where the location of the four-point reflections along the fiber axis is denoted as $|s_{3LM}|$. The lateral long-spacing, $L_{12} = |1/s_{12LM}|$, between crystals was then calculated from the transversal peak positions, $|s_{12LM}|$. For the tilted lamellae model, the tilt-angle of lamellae with respect to the filament axis can be calculated as follows.

$$\varphi = \pm \arctan\left(\frac{s_{12LM}}{s_{3LM}}\right) = \pm \arctan\left(\frac{L_3}{L_{12}}\right) \quad (\text{Eq. 7})$$

3. Results and discussion

3.1. Raman mapping

Raman maps have been measured across the face of all fibers. The assignments of relevant Raman bands to vibrations in PET are summarized in Table 2.

As mentioned in the experimental section, all Raman spectra from PET have been normalized to the peak at 1291 cm⁻¹, which is arising from a ring and O–C stretching. It is necessary to perform this normalization procedure to eliminate changes in the intensity due to e.g. a bent fiber surface. The same normalization procedure has already been successfully applied previously [9]. Three spectral regions have been analyzed, that comprise the following four Raman bands: 1097, 1120,

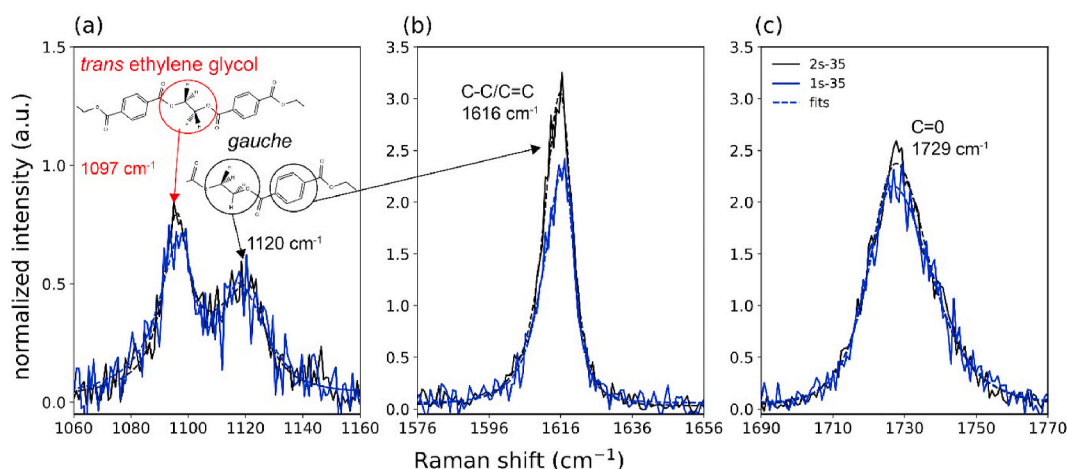


Fig. 3. Binned Raman spectra in the center of fiber cross-sections (2s-35 and 1s-35). Three spectral regions were fitted comprising the Raman bands at (a) 1097, 1120 cm⁻¹, (b) 1616 cm⁻¹ and (c) 1729 cm⁻¹.

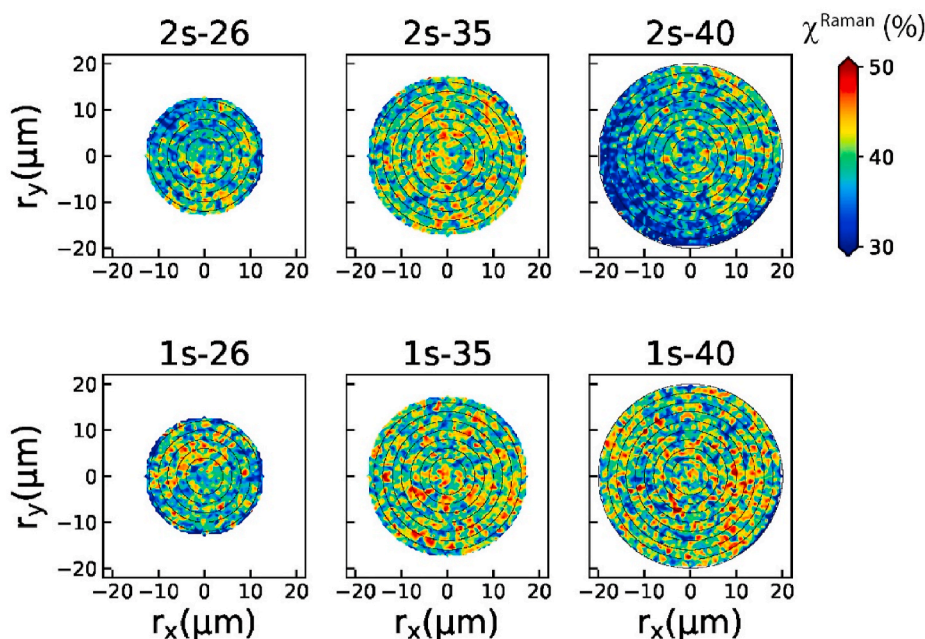


Fig. 4. Calculated Raman crystallinity, $\chi^{\text{Raman}}(\%)$, maps of fiber cross-sections. Top row: 2-step drawn fibers. Bottom row: 1-step drawn fibers. The integrated annuli of 2 μm in width are shown as black circles.

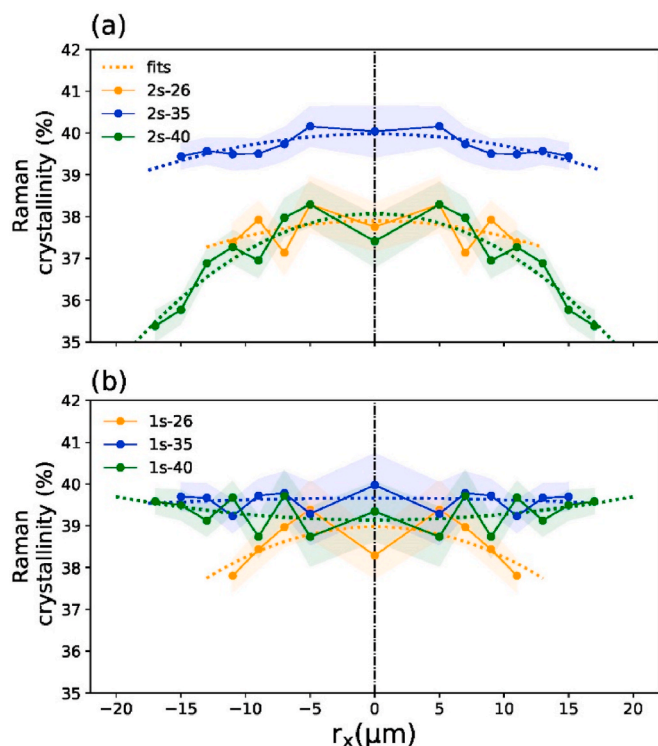


Fig. 5. Symmetrized radial crystallinity gradients. Polynomial fits are shown as dotted lines. (a) 2-step drawn fibers and (b) 1-step drawn fibers. Errorbars of Raman crystallinities are shown as shaded areas, they have been extracted through error propagation of peak fit errors.

1616 and 1729 cm^{-1} . The normalized Raman intensities are shown in Fig. 3 for the fiber samples 2s-35 and 1s-35. Each Raman band has been fitted to a split Pearson VII function. As can be seen from Fig. 3, the fits (dashed curves) perform well.

The ethylene glycol segment is known to adopt a *trans* conformation in the crystalline phase of PET and gives rise to a Raman band at 1097 cm^{-1} , as is shown in Fig. 3a. In the amorphous phase, however, both

gauche and *trans* conformations are present [17–19,22–26]. The *gauche* conformation gives rise to a Raman band at 1120 cm^{-1} (Fig. 3a). The peak heights of these two bands can be used to determine PET crystallinities using equation (2). The Raman band at 1616 cm^{-1} (Fig. 3b) arises from the symmetric stretching of the 1,4-carbons of the benzene ring [27] and is reflecting the molecular orientation of polymer chains [27–30]. The 1729 cm^{-1} (Fig. 3c) Raman band arises from the C=O stretching. Mainly its width is of interest since it is inversely correlated with the crystallinity of PET [9].

The obtained crystallinity maps from analyzing the 1097 and 1120 cm^{-1} Raman bands for all fiber cross-sections are shown in Fig. 4. Interconnected networks of crystalline strands within low crystalline matrices are observed, similar to previous observations for other PET fibers [9]. It is also observed that 2-step drawn fibers show less radial symmetry than 1-step drawn fibers. For 2-step drawn fibers this non-uniformity may be a result of the drawing over a heating plate.

Radial gradients in the crystallinities have been calculated by averaging the crystallinity values in annuli of 2 μm width and are shown in Fig. 5. For the 2-step drawn fibers (Fig. 5a), the crystallinity is decreasing towards the fiber surface (2s-40, 38.1%–35.4%), whereas for the thicker 1-step drawn fibers (Fig. 5b), the crystallinity is weakly increasing (1s-40, 39.1%–39.6%) towards the fiber surface. The given crystallinity values refer to the values extracted from the fitted polynomial function. For 2-step drawn fibers, the fiber is wound up directly after melt-spinning, later followed by a drawing of the conditioned fiber over a heating plate. In this case, the core of the fiber is drawn at a colder temperature than the surface region of the fiber, which enhances the stress-induced crystallization in the core. For 1-step drawn fibers, on the other hand, the fiber is drawn directly online during melt-spinning, and the surface cools down first, which enhances the stress-induced crystallization in the surface region of the fiber. For the thinnest sample, 1s-26 μm , the melt strand cools down and solidifies the fastest, and is most likely heated back up in the online drawing, which may be the reason why an opposite trend is observed in the radial gradient of the crystallinity for this particular sample. Note that this sample has also been melt-spun with a different capillary die and take-up speed, in order to achieve a fine filament using the same draw ratio.

Additionally, we have analyzed the intensity of the 1616 cm^{-1} Raman band of the normalized spectra. The corresponding Raman maps

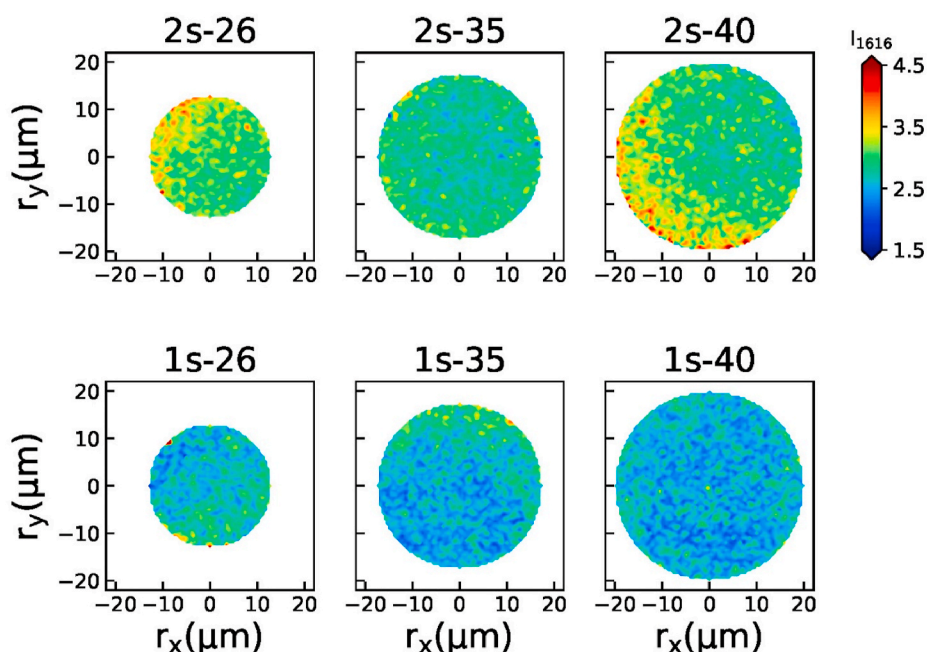


Fig. 6. Intensity maps of the 1616 cm^{-1} Raman band. Top row: 2-step drawn fibers. Bottom row: 1-step drawn fibers.

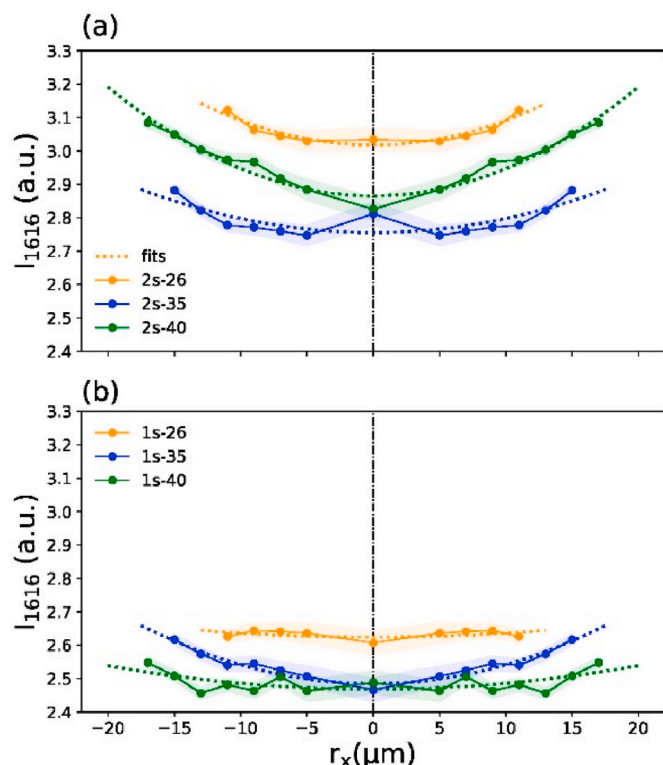


Fig. 7. Symmetrized radial gradients of the 1616 cm^{-1} Raman band intensity. (a) 2-step drawn fibers and (b) 1-step drawn fibers. Errorbars of the measured average radial intensities are shown as shaded areas.

are shown in Fig. 6. As mentioned before, this Raman band corresponds to the benzene ring mode and reflects the molecular chain orientation. The incident laser light onto the sample is linearly polarized in the plane of the sample and thus only benzene rings that lie in the plane of the sample contribute to the 1616 cm^{-1} Raman band signal. Thus, if the chains lie out-of-plane along the fiber axis, the benzene rings lie also along the fiber axis, leading to a smaller 1616 cm^{-1} Raman band signal [31–33]. Therefore, the higher the 1616 cm^{-1} intensity, the lower is the orientation of the molecular chains. From Fig. 6, one can therefore deduce that 2-step drawn fibers have less oriented chains than 1-step drawn fibers, which most likely correlates with the smaller draw ratio of 2-step drawn fibers. Interestingly, the regions of less orientation (high intensity) correlate with the low crystallinity regions in Fig. 4. This signifies that the molecular chains are less oriented in regions that undergo less stress-induced crystallization.

The symmetrized radial gradients of the Raman band intensity 1616 cm^{-1} are shown in Fig. 7. The analysis shows that the core is more oriented than the surface region, especially for the 2-step drawn fibers. Less pronounced radial gradients are observed for the 1-step drawn fibers. The explanation why the molecular alignment is higher in the core than at the surface of PET fibers is not straightforward, because many

Table 3

Average values extracted from Raman maps: crystallinity, FWHM of 1729 cm^{-1} and intensity of 1616 cm^{-1} Raman band. Standard deviations were calculated from all the spectra in the fiber cross-sections.

	χ Raman (%)	FWHM 1729 cm^{-1} (cm^{-1})	Intensity 1616 cm^{-1} (a.u.)
2s-26	37 ± 5	21.2 ± 0.7	3.1 ± 0.2
2s-35	39 ± 5	20.6 ± 0.7	2.8 ± 0.2
2s-40	36 ± 6	21.4 ± 1.0	3.0 ± 0.3
1s-26	38 ± 7	21.4 ± 0.9	2.7 ± 0.3
1s-35	39 ± 5	21.1 ± 0.7	2.6 ± 0.2
1s-40	39 ± 5	21.1 ± 0.9	2.5 ± 0.2

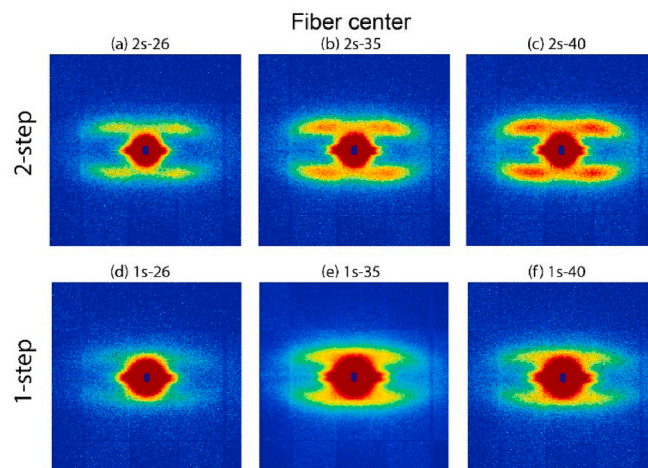


Fig. 8. Averaged SAXS patterns from the central region ($r < 2\text{ }\mu\text{m}$) of the fibers. Note that the measured patterns have been treated through cropping, transposing and symmetrizing operations (supporting information, section 3).

factors influence the molecular alignment during the spinning and drawing procedures, like for example solidification stress and necking (squeezing deformation), internal shear due to temperature gradients, shear imposed onto the surface by godets or heating plates, as well as stress-induced crystallizations and tilts of crystals thereof [34].

The extracted average values of the crystallinities, full width at half maximum (FWHM) of the 1729 cm^{-1} Raman band, and the intensity of the 1616 cm^{-1} Raman band, are summarized in Table 3. Note that the average Raman crystallinity values match well with values extracted from differential scanning calorimetry measurements (supporting information, SI section 2, Table 1). The Raman maps and radial gradients of the FWHM of the 1729 cm^{-1} band are shown in the supporting information (SI, Fig. 1). A lower crystallinity often correlates with a higher FWHM of the 1729 cm^{-1} band and vice versa [9,22]. The FWHM is increasing towards the fiber surface for the 2-step drawn fibers, and is decreasing towards the fiber surface for the 1-step drawn fiber, 1s-40 (supporting information, SI Fig. 2). Thus, these observed trends for the FWHM of the 1729 cm^{-1} band confirm the observed radial trends for the crystallinity (supporting information, section 1.1.). The average intensity of the 1616 cm^{-1} Raman band in Table 3 shows that the 2-step drawn fibers have less oriented molecules (higher intensity values), which is most likely a result of the lower draw ratio.

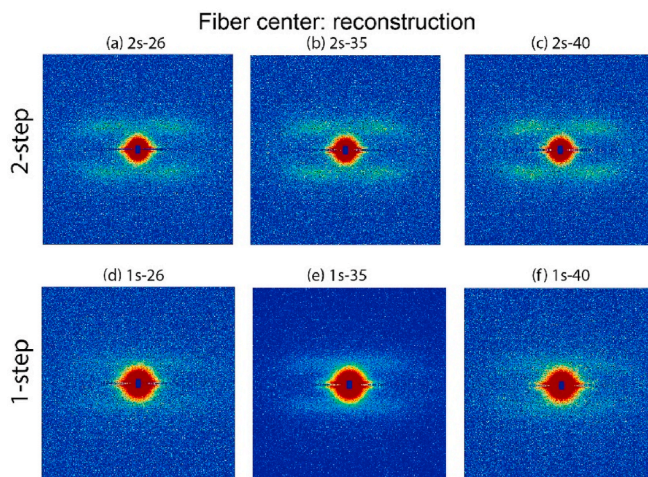


Fig. 9. Reconstructed averaged SAXS images from the central region ($r < 6\text{ }\mu\text{m}$) of the fibers using the Basex algorithm.

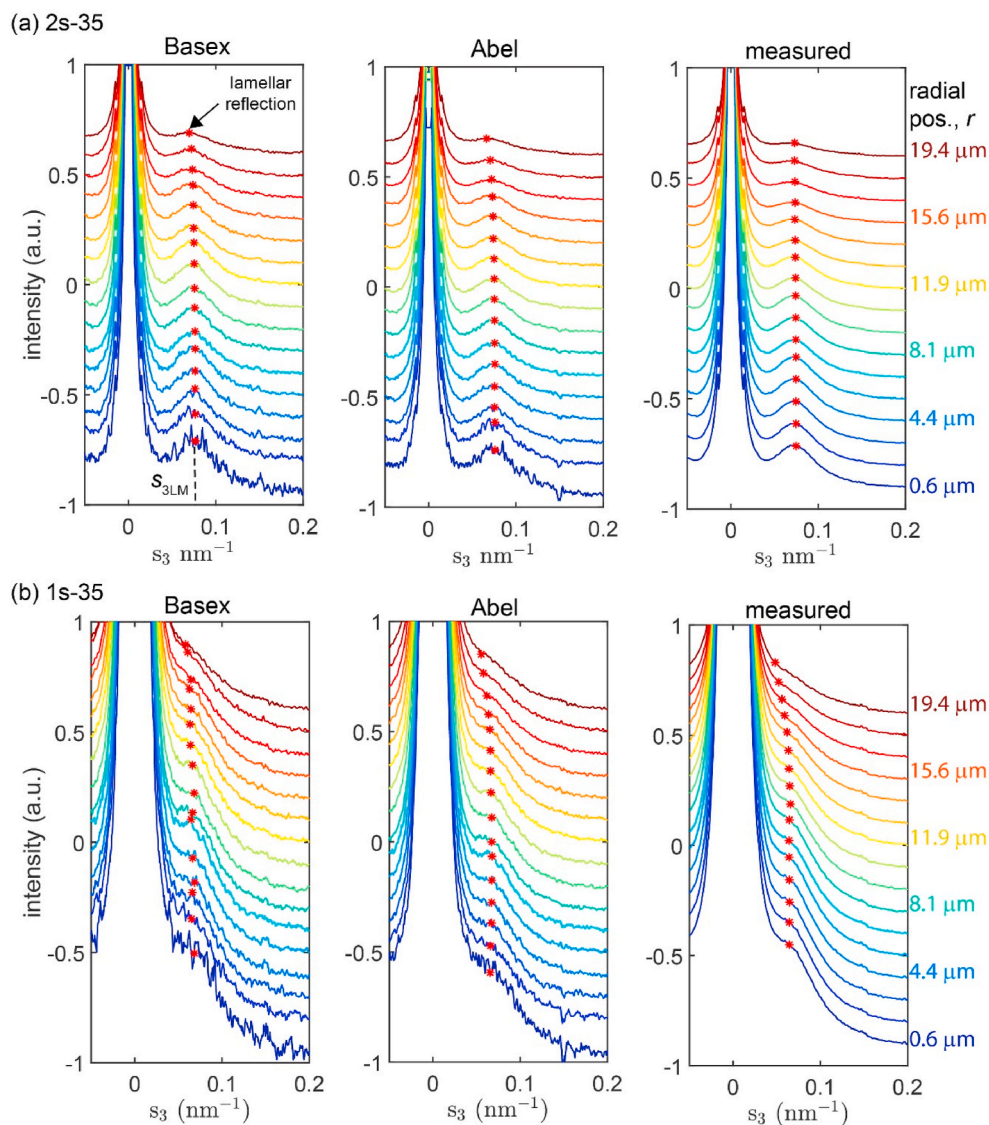


Fig. 10. Meridional profiles extracted from binned reconstructed (Basex or two-point Abel algorithms) and measured SAXS patterns for different radial positions (step size 1.25 μm) for fiber (a) 2s-35 and (b) 1s-35. Stars indicate the found meridional lamellar positions, $s_{3\text{LM}}$.

3.2. Microbeam SAXS tomography

One-dimensional microbeam SAXS tomography was performed to obtain complementary information about long-spacings (spacing between crystals) and crystal tilts. Long-spacings are expected to be correlated with the draw ratio and thus tensile properties of the fiber. Measured SAXS patterns from the center of the fiber (averaged over 2 images, $r < 2 \mu\text{m}$) are shown in Fig. 8. For details about the data treatments, the reader is referred to the experimental section and the supporting information (SI, section 3). The SAXS patterns in Fig. 8 show that there is a clear difference between the 2-step and 1-step drawn PET filaments. The 2-step drawn filaments have quite a strong 4-point pattern, whereas filaments, which have been drawn online (1-step), show a weaker pattern and the reflections are vertically located closer to the direct beam.

Corresponding reconstructed images (averaged over 5 images, $r < 6 \mu\text{m}$), using the BASEX algorithm, are shown in Fig. 9. The weak scattering of PET crystals, as well as the small scattering volume due to the fineness of the fibers ($\leq 40 \mu\text{m}$), lead to a low signal-to-noise ratio in the reconstructed SAXS patterns. To enhance the signal-to-noise ratio, and thus to better visualize the scattering in the reconstructed images, the images have been averaged over a larger central region ($r < 6 \mu\text{m}$). Note

that one sample, 1s-35, was measured with more scans and longer exposure times (10 scans with 1s, and 10 with 2s) and thus the signal-to-noise ratio for this particular filament is improved.

The averaged SAXS patterns from the edge region (supporting information, SI Fig. 8) are weaker and reflections appear to be closer to the meridian. Fig. 10 shows the meridional profiles extracted from the reconstructed images (Basex, Abel) and the measured images from the center of the fiber ($r = 0$) up to its surface for (a) the 2s-35 sample and (b) the 1s-35 sample. The red stars indicate the fitted lamellar peak positions, $s_{3\text{LM}}$, through fits with Pearson VII functions. For both fibers, the lamellar reflections move towards the direct beam, which indicates an increase in the long-spacing, L_3 . Fits of transversal profiles to extract the transversal long-spacing, L_{12} , are shown in the supporting information (SI Fig. 6).

The gradients in the long-spacings L_3 and L_{12} , and crystal tilt angles for fiber samples 2s-35 and 1s-35, are shown in Fig. 11 for measured, Abel and Basex reconstructed images. Overall, the measured images, as well as Abel and Basex reconstructed images, give very similar results. For the 2s-35 fiber, the long-spacings and crystal tilts are rather constant. In the case of the 1-step fiber, however, the long-spacings increase towards the fiber surface.

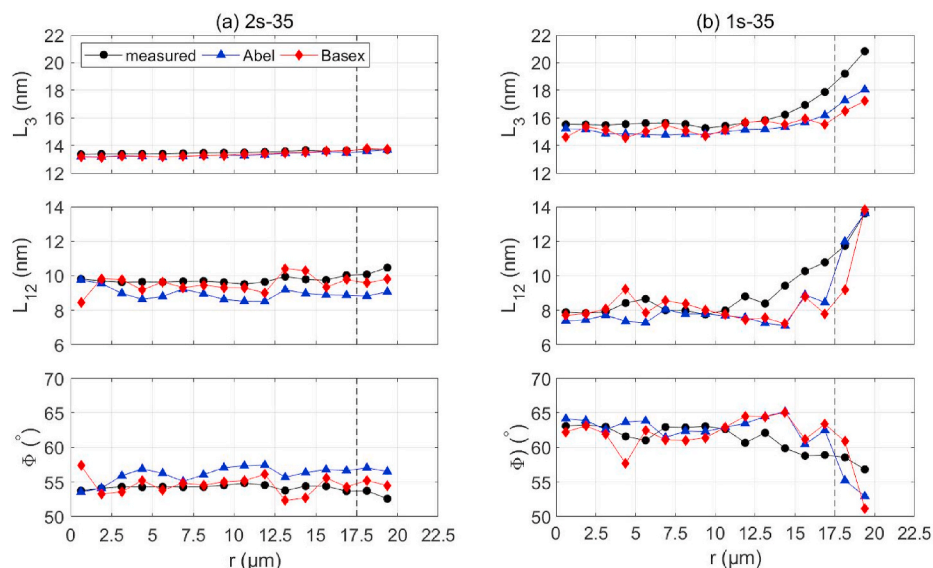


Fig. 11. Determined long-spacings along the fiber axis, L_3 , and perpendicular to it, L_{12} , as well as calculated tilt angles for fiber samples (a) 2s-35 and (b) 1s-35. Vertical dashed lines indicate the position of the fiber surface. If the center of the x-ray beam is located above the radial position of the fiber surface, then only the tails of the beam hit the fiber surface.

Overplots of the radial changes in long-spacings, and tilts with respect to the core, are shown for all fiber samples in Fig. 12. Overall, most fibers show a slight increase in the long-spacing L_3 towards the surfaces of the fibers, which may be a result of necking, or of larger internal shear forces towards the surface. Note that the vertical dashed lines in Fig. 12 indicate the position of the fiber surfaces, thus data points slightly to the left or right of the vertical dashed lines indicate the positions where the x-ray beam only partially hit the fiber.

L_{12} shows a slightly decreasing trend for the 2-step fibers towards the surface, whereas for the 1-step drawn fibers it is slightly increasing. This results in tilts of the lamellae for the 2-step drawn fibers that are slightly increasing towards the fiber surface, but are rather decreasing for the 1-step drawn fibers. With Raman, it was observed that the molecular alignment is generally decreasing towards the fiber surface, which suggests that a smaller crystal tilt correlates with a lower molecular alignment. 2-step drawn fibers generally show a smaller crystal tilt (Fig. 11) than 1-step drawn fibers, while Raman data has shown a smaller molecular

alignment of the 2-step drawn fibers (Fig. 7).

One has to be careful with the interpretation of the results from one-dimensional SAXS tomography, because the reconstruction is based on the assumption of radial symmetry. Raman mapping results have shown, that the 2-step drawn fibers are not completely radially symmetric. The non-uniformity of the fiber may result in a slightly falsified picture of the radial gradient of structural data obtained by 1D SAXS, e.g. a less pronounced gradient than the effective gradient in the filament. One has also to be aware that the x-ray beam hits several micrometers of the fiber, and thus local radial asymmetries can be below the detection limit. Nevertheless, the consistent trend that long-spacings, L_3 , are slightly increasing towards the surface, suggests that this is indeed the case.

The average long-spacings and tilts are shown in Fig. 13. Due to the higher draw ratios of the 1-step drawn fibers ($DR = 5.2$), the long-spacing, L_3 , is larger than for the 2-step drawn fibers ($DR = 4.6$), and the L_{12} is smaller for the 1-step fibers, since the crystals are pushed together in the lateral direction. This effect is most likely also causing

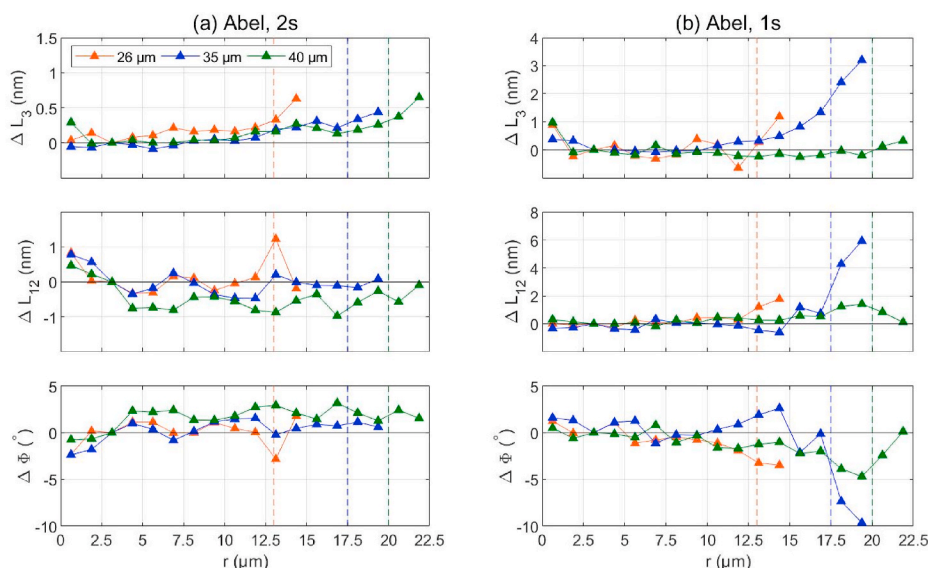


Fig. 12. Changes in long-spacings and tilt angles with respect to the core of the fiber, for (a) 2-step drawn fibers and (b) 1-step drawn fibers.

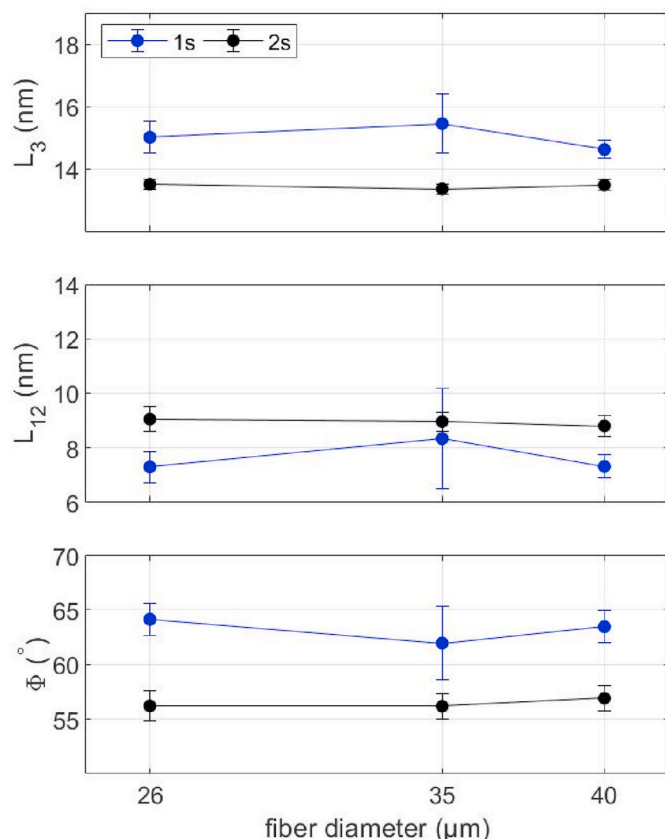


Fig. 13. Calculated average long-spacings and tilts for all fibers based on the Abel reconstructed images. The error bars indicate the standard deviations calculated from the values at different radial positions.

the lamellae of the 1-step drawn fibers to be more tilted. The larger long-spacing in 1-step drawn filaments correlates with a higher tensile strength (~ 58 cN/tex) and a lower elongation at break (19%) compared to 2-step drawn filaments (~ 54 cN/tex, 25%).

4. Conclusion

High-resolution Raman mapping was used to investigate radial structures in differently drawn and melt-spun PET filaments. The crystallinity has been successfully extracted from the Raman bands that are associated with the *trans* and *gauche* conformation of the ethylene glycol segments in PET. Raman maps have revealed that 2-step drawn filaments have a higher crystallinity in the core, whereas the thicker 1-step drawn filaments ($\phi = 35, 40 \mu\text{m}$) have shown the opposite trend. Stress-induced crystallization occurs mainly in the core for the 2-step drawn fibers, whereas for 1-step drawn fibers, it mainly happens at the surface. The radial gradients in the FWHM of the 1729 cm^{-1} Raman band (C=O stretching mode) have shown an inverse correlation with gradients in crystallinity. The molecular alignment was extracted from the 1616 cm^{-1} Raman band (benzene ring mode) and has been found to be the highest (low peak intensity) in the core for all samples. Various factors can influence the radial profile of the molecular alignment, such as necking, internal shear due to temperature gradients, shear imposed onto the surface by godets or heating plates, and stress-induced crystallization. On average, the 1-step drawn fibers have shown a higher molecular alignment than 2-step drawn fibers, which is most likely a result of the higher draw ratio of the 1-step drawn fibers. Note that in previous publications, high molecular alignments have also been correlated with the presence of mesophases (highly oriented non-crystalline molecular chains along the fiber axis) [9,35–38]. For the future, it would be interesting to analyze cross-sections taken along the fiber axis in order to study the longitudinal microstructure.

1D microbeam SAXS has revealed that the long-spacing between crystals along the fiber axis is increasing towards the fiber surface for all fibers, and that the transversal long-spacing is slightly decreasing for 2-step drawn fibers, but increasing for the 1-step drawn fibers. The increase of the long-spacing along the fiber axis may also be explained through necking or larger shear forces that occur at the fiber surface. This gradient in long-spacing might affect the toughness of the surface.

Funding sources

Part of this work was funded by the Swiss Innovation Agency Innosuisse (project number: 26744.1).

CRediT authorship contribution statement

E. Perret: Software, Formal analysis, Investigation, Data curation, Writing – original draft, Visualization. **K. Chen:** Data curation. **O. Braun:** Data curation, Writing – review & editing. **R. Muff:** Data curation. **R. Hufenus:** Supervision, Project administration, Writing – review & editing.

Declaration of competing interest

The authors declare that they have no known competing financial interests or personal relationships that could have appeared to influence the work reported in this paper.

Acknowledgment

We would like to thank Prof. Dr. M. Calame for providing access to the Raman microscope at Empa Dübendorf, Switzerland. We also thank Dr. A. Menzel for his support during the beamtime at the Swiss Light Source, PSI, Switzerland. We thank Dr. A. Gooneie for helpful discussions as well as Prof. Dr. M. Heuberger for his participation during the beamtime and Dr. P. Kraft for providing us the Matlab codes, which we have adapted for our purposes. We acknowledge Dr. N. Stribeck for making all of his algorithms available on the web. We also thank Dr. H. Reisler and Dr. B. Karpichev for providing the Basex Matlab algorithm.

Appendix A. Supplementary data

Supplementary data to this article can be found online at <https://doi.org/10.1016/j.polymer.2021.124422>.

References

- [1] M. Jaffe, A.J. Easts, X. Feng, 8 - polyester fibers, in: M. Jaffe, J.D. Menczel (Eds.), *Thermal Analysis of Textiles and Fibers*, Woodhead Publishing, 2020, pp. 133–149.
- [2] P. Kraft, et al., One-dimensional small-angle X-ray scattering tomography of dip-coated polyamide 6 monofilaments, *J. Synchrotron Radiat.* 17 (2) (2010) 257–262.
- [3] N. Stribeck, Analysis of SAXS fiber patterns by means of projections, in: *Scattering from Polymers*, American Chemical Society, 1999, pp. 41–56.
- [4] N. Stribeck, X-ray scattering for the monitoring of processes in polymer materials with fiber symmetry, *Polym. Rev.* 50 (1) (2010) 40–58.
- [5] C.J. Dasch, One-dimensional tomography: a comparison of Abel, onion-peeling, and filtered backprojection methods, *Appl. Opt.* 31 (8) (1992) 1146–1152.
- [6] V. Dribinski, et al., Reconstruction of Abel-transformable images: the Gaussian basis-set expansion Abel transform method, *Rev. Sci. Instrum.* 73 (7) (2002) 2634–2642.
- [7] J. Shimizu, N. Okui, T. Kikutani, Fine structure and physical properties of fibers melt-spun at high speeds from various polymers, in: A. Ziabicki, H. Kawai (Eds.), *High-speed Fiber Spinning*, John Wiley & Sons, New York, 1985, pp. 429–483.
- [8] S. Natarajan, S. Michielsen, Using confocal Raman microscopy to determine the structure and orientation of the PET interior of PET/PP core/shell fibers, *Textil. Res. J.* 69 (12) (1999) 903–907.
- [9] E. Perret, et al., High-resolution 2D Raman mapping of mono- and bicomponent filament cross-sections, *Polymer* 229 (2021) 124011.
- [10] K. Sharma, et al., 2D Raman, ATR-FTIR, WAXD, SAXS and DSC data of PET mono- and PET/PA6 bicomponent filaments, *Data in Brief* 38 (2021) 107416.
- [11] B. Henrich, et al., PILATUS: a single photon counting pixel detector for X-ray applications, *Nucl. Instrum. Methods Phys. Res. Sect. A Accel. Spectrom. Detect. Assoc. Equip.* 607 (1) (2009) 247–249.

- [12] N. Stribeck, U. Nöchel, A. Almendárez Camarillo, Scanning microbeam X-ray scattering of fibers analyzed by one-dimensional tomography, *Macromol. Chem. Phys.* 209 (19) (2008) 1976–1982.
- [13] W. Fronk, W. Wilke, Small angle scattering of partially oriented polymers: model calculations with monoclinic macrolattice, *Colloid Polym. Sci.* 263 (2) (1985) 97–108.
- [14] E. Perret, et al., Modified crystallization in PET/PPS bicomponent fibers revealed by small-angle and wide-angle X-ray scattering, *Macromolecules* 46 (2) (2013) 440–448.
- [15] N.S. Murthy, D.T. Grubb, Deformation in lamellar and crystalline structures: in situ simultaneous small-angle X-ray scattering and wide-angle X-ray diffraction measurements on polyethylene terephthalate fibers, *J. Polym. Sci. B Polym. Phys.* 41 (13) (2003) 1538–1553.
- [16] N.S. Murthy, D.T. Grubb, Tilted lamellae in an affinely deformed 3D macrolattice and elliptical features in small-angle scattering, *J. Polym. Sci. B Polym. Phys.* 44 (8) (2006) 1277–1286.
- [17] F.J. Boerio, S.K. Bahl, G.E. McGraw, Vibrational analysis of polyethylene terephthalate and its deuterated derivatives, *J. Polym. Sci. Polym. Phys. Ed* 14 (6) (1976) 1029–1046.
- [18] T. Lippert, F. Zimmermann, A. Wokaun, Surface analysis of excimer-laser-treated polyethylene-terephthalate by surface-enhanced Raman scattering and X-ray photoelectron spectroscopy, *Appl. Spectrosc.* 47 (11) (1993) 1931–1942.
- [19] A.J. Melveger, Laser-Raman study of crystallinity changes in poly(ethylene terephthalate), *J. Polym. Sci. 2 Polym. Phys.* 10 (2) (1972) 317–322.
- [20] R. Paquin, M.-H. Limage, P. Colombari, Micro-Raman study of PET single fibres under high hydrostatic pressure: phase/conformation transition and amorphization, *J. Raman Spectrosc.* 38 (9) (2007) 1097–1105.
- [21] E.B. Wilson, The normal modes and frequencies of vibration of the regular plane hexagon model of the benzene molecule, *Phys. Rev.* 45 (10) (1934) 706–714.
- [22] B.J. Bulkin, M. Lewin, F.J. DeBlase, Conformational change, chain orientation, and crystallinity in poly(ethylene terephthalate) yarns: Raman spectroscopic study, *Macromolecules* 18 (12) (1985) 2587–2594.
- [23] F.J. Deblase, et al., Low-frequency Raman spectra of poly(ethylene terephthalate), *J. Polym. Sci., Polym. Lett. Ed.* 23 (2) (1985) 109–115.
- [24] G. Ellis, et al., FT Raman study of orientation and crystallization processes in poly(ethylene terephthalate), *Spectrochim. Acta Mol. Biomol. Spectrosc.* 51 (12) (1995) 2139–2145.
- [25] N. Everall, et al., Study of density and orientation in poly(ethylene terephthalate) using Fourier transform Raman spectroscopy and multivariate data analysis, *Polymer* 35 (15) (1994) 3184–3192.
- [26] S.-B. Lin, J.L. Koenig, Spectroscopic characterization of the rotational conformations in the disordered phase of poly(ethylene terephthalate), *J. Polym. Sci. Polym. Phys. Ed* 20 (12) (1982) 2277–2295.
- [27] J. Purvis, D.I. Bower, I.M. Ward, Molecular orientation in PET studied by polarized Raman scattering, *Polymer* 14 (8) (1973) 398–400.
- [28] D.A. Jarvis, et al., Characterization of biaxial orientation in poly(ethylene terephthalate) by means of refractive index measurements and Raman and infrared spectroscopies, *Polymer* 21 (1) (1980) 41–54.
- [29] C.C.C. Lesko, et al., Experimental determination of the fiber orientation parameters and the Raman tensor of the 1614cm⁻¹ band of poly(ethylene terephthalate)☆In honour of Professor Giuseppe Zerbi on the occasion of his 65th birthday.☆, *J. Mol. Struct.* 521 (1) (2000) 127–136.
- [30] S. Yang, S. Michielsen, Orientation distribution functions obtained via polarized Raman spectroscopy of poly(ethylene terephthalate) fibers, *Macromolecules* 36 (17) (2003) 6484–6492.
- [31] D.I. Bower, Investigation of molecular orientation distributions by polarized Raman scattering and polarized fluorescence, *J. Polym. Sci. Polym. Phys. Ed* 10 (11) (1972) 2135–2153.
- [32] N.J. Everall, Measurement of orientation and crystallinity in uniaxially drawn poly(ethylene terephthalate) using polarized confocal Raman microscopy, *Appl. Spectrosc.* 52 (12) (1998) 1498–1504.
- [33] M. Richard-Lacroix, C. Pellerin, Accurate new method for molecular orientation quantification using polarized Raman spectroscopy, *Macromolecules* 46 (14) (2013) 5561–5569.
- [34] R. Hufenus, et al., Melt-spun fibers for textile applications, *Materials* 13 (19) (2020).
- [35] E. Perret, R. Hufenus, Insights into strain-induced solid mesophases in melt-spun polymer fibers, *Polymer* 229 (2021) 124010.
- [36] E. Perret, F.A. Reifler, A. Gooneie, K. Chen, F. Selli, R. Hufenus, Structural response of melt-spun poly(3-hydroxybutyrate) fibers to stress and temperature, *Polymer* 197 (2020) 122503.
- [37] E. Perret, F.A. Reifler, A. Gooneie, R. Hufenus, Tensile study of melt-spun poly(3-hydroxybutyrate) P3HB fibers: Reversible transformation of a highly oriented phase, *Polymer* 180 (2019) 121668.
- [38] E. Perret, K. Sharma, S. Tritsch, R. Hufenus, Reversible mesophase in stress-annealed poly(3-hydroxybutyrate) fibers: A synchrotron x-ray and polarized ATR-FTIR study, *Polymer* 231 (2021) 124141.